CEAS-GNC-2022-016

CEAS EuroGNC 2022
"Conference on Guidance, Navigation and Control"
3-5 May 2022 @ Technische Universität Berlin, Germany

Visual Odometry Fusion with GNSS/IMU Localization of UAVs in Urban Areas and Integrity Monitoring

Mats Martens Research Assistant, Technische Universität Berlin, Chair of Flight Guidance and Air Transport, 10587, Berlin, Germany. martens@tu-berlin.de

ABSTRACT

Urban environments represent a challenging area for UAVs as part of Urban Air Mobility. The reliance on the conventional fusion of GNSS and INS may not fulfill the higher navigation specifications, which could be issued by authorities due to the increased risk of urban air operation. Within this paper, GNSS measurements are fused with those of a consumer grade IMU and VO derived measurements of a monocular camera setup. The intention is to monitor the integrity of the filter solutions and to increase the continuity compared to the conventional fusion. For that purpose, a novel filter architecture is presented, comprising an INS/GNSS and an INS/VO Extended Kalman Filter running in parallel. Using integrity monitoring strategies, unreliable, redundant pseudo-range measurements can be rejected within the INS/GNSS filter through Innovation Filtering. Additionally, the integrity of both filters is monitored using a χ^2 test statistic and a $\mathscr{H}_0$ hypothesis test. Once the INS/GNSS filter solution is detected as unreliable, the INS/VO filter bridges the outage until the INS/GNSS filter recovered. By fusing the IMU measurements with those of the VO algorithm, the drift can be drastically reduced. Finally, the proposed filter architecture is applied to a recorded test dataset and the assumed benefits are verified. While the accuracy of the parallel design is proven to be qualitatively better than the individual filters alone, the proposed filter doubles the continuity property of the navigation solution.

Keywords: Visual Odometry; Integrity Monitoring; UAV Navigation; Sensor Fusion; Kalman Filter

1 Introduction

As the main applications of the growing number of UAVs will be within the urban environment, the air traffic will be concentrated above densely populated areas [1]. Due to the associated increased risk for the population, more stringent navigation requirements may be needed.

Within their Performance Based Navigation (PBN) document, the ICAO introduced PBN, which defines operational navigation requirements by navigation specifications [2]. Hereby, specifications may either be Area Navigation (RNAV) or Required Navigation Performance (RNP), where the latter additionally incorporates on-board performance monitoring and alerting functionalities. In order to qualify for RNAV or RNP navigation specifications, ICAO prescribes navigation systems to meet a set of accuracy, integrity, availability and continuity requirements.

Currently, different companies and interest groups are developing ideas for future airspace designs, for example see [3], [4], [5]. For example, aircraft entering managed air traffic zones following the U-space are suggested by SESAR Joint Undertaking to meet the Required U-space Navigation Performance RUNP-5m navigation specification, which requires the navigation equipment to ensure an accuracy of $\pm 5m$ and an integrity of greater than $1 - 1 \times 10^{-7}h$ with a Time-To-Alert of less than 1 second.

Furthermore, existing navigation systems face new challenges within the urban environment. These systems mainly rely on GNSS for its coverage, accuracy and costs [6]. However, these benefits require open-sky conditions and reveal new challenges for GNSS based aircraft navigation in urban areas by representing GNSS challenging or even GNSS denied environments [7]. At low heights, GNSS performance is prone to errors, caused by masking and multipath errors, which can lead to biases of up to 70 meters [8].

Combining higher requirements for urban airspace, defined by future airspace concepts, and the challenges for existing navigation systems within the urban environment, mitigations must be identified to overcome the GNSS degradation in urban areas.

Currently, related work focuses either on the elaboration of alternatives of GNSS in urban areas or to integrate additional sensors into the navigation systems. The FAA suggests an optimized DME network, Wide-Area Multilateration and a Pseudolite network as three alternative navigation systems in [9]. All these systems use ground based infrastructure. Especially Pseudolite networks, which transmit signals similar to GNSS, can improve the vertical position estimation and suffer less from atmospheric errors [10]. Another study concludes that "multi-sensor navigation is one of the most promising complementary solutions" [1, p. 2] to enhance GNSS based navigation, while GNSS still remains the reference navigation system. The authors summarize the alternative navigation systems as Inertial Sensors, LIDAR, odometers, magnetometers as well as vision based measurements and the ground based systems, introduced by the FAA. Additionally, a-priori information can be added e.g. by aiding LIDAR and GNSS measurements with 3D environment maps [6]. As GNSS shall remain the reference navigation system, one important task of additional sensors is to provide GNSS performance monitoring as well as performance prediction and sensor switching [1].

Within this work, a parallel filter integration of multiple sensors is proposed. Hereby, a camera with a monocular VO algorithm is fused with an existing IMU and GNSS fusion algorithm. Additionally, integrity monitoring functionalities are provided. A mode switching logic is developed to switch to dead reckoning fusion, if GNSS positioning is unreliable. A χ^2 test statistic ensures the overall integrity of both filters.

The filter design follows a similar approach to the work of Groves [7] and Wendel [8], while the Visual Odometry concepts are based on the work of Szeliski [11] and Corke [12].

2 Sensor and Data Source Limitations

This section primarily aims on introducing error sources of the specific sensor types and data sources and how to model them in order to incorporate them within a navigation filter.

2.1 Inertial Measurement Unit

IMUs measure specific forces f_{ib}^{b} and angular rates ω_{ib}^{b} of the body frame relative to the inertial frame within the body frame. Using Strapdown Integration, those values can be integrated to obtain the pose (position and orientation) and the velocity (e.g. within the earth frame as r_{eb}^{e}, C_{b}^{e} and v_{eb}^{e}), which forms an INS. Navigation based on IMU, Inertial Navigation, is used because of the fault characteristics, high update rate of more than 50Hz and low short-term noise [7].

Bias drifts $\dot{b}_a$ and $\dot{b}_g$ can be modeled in three different ways. For high quality IMUs, biases are considered to be stable, i.e. the bias drift is zero $\dot{b}_a = \dot{b}_b = 0$ [8]. If the bias drift can not be neglected, it can either be modeled as a first order Gauß-Markov-Process or a Random-Walk Process [8]. As the velocity and the position are integrated from both measured values, their errors grow with time. Especially, the integration of random noise leads to random-walk errors within the integrated dimensions.

IMUs can be divided into marine, aviation, intermediate, tactical and consumer grade IMUs, which differ in quality, but also in their costs [7]. Typical accelerometer biases for consumer grade IMUs are $> 0.03\,ms^{-2}$ and for aviation grade IMUs $3 \times 10^{-4}\,ms^{-2}$. However, the author also mentions the difference in costs associated with different grades, i.e. 8€ for consumer grade and 80 000€ for aviation grade IMUs.

2.2 Global Navigation Satellite System

GNSS are navigation systems that enable a user to localize himself within the 3-D space by receiving radio-frequency (RF) signals from orbiting satellites. These systems consist of a space, a ground and a user segment. The space segment of a navigation system comprises satellites or SV, which, in their entirety, are called constellation. Currently, there are different constellations of satellites orbiting the earth and providing global coverage, namely GPS, GLONASS, BeiDou and Galileo [13].

As introduced in Section 1, urban environments represent areas with large structures, which can reflect or block the GNSS RF signals. The reception of a reflected signal is referred to as NLOS reception. Structures that prevent a line-of-sight (LOS) reception create a volume between them and the antenna, which is called shadow.

Figure 1 shows recorded measurements from a driving car with the associated camera frame shown in Figure 7 within the Appendix. The shadows reach elevation angles of up to 46 degrees. It can be seen that no constant masking angle can be defined to simultaneously exclude the NLOS SV and keep the LOS SV. Making the masking angle dependent on the location and azimuth angle is a known technique called Shadow Matching, where a 3-D city model is used as reference. For further reading on Shadow Matching see [14].

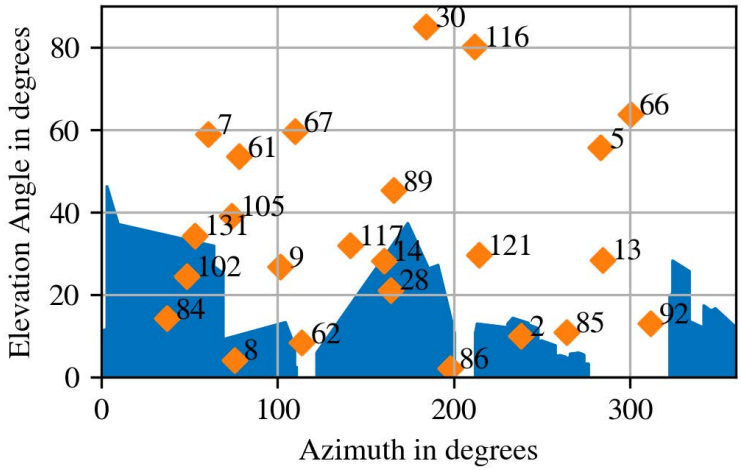

Fig. 1 Azimuth and elevation plot of SV (orange) and their ID with urban structures (blue) throwing a shadow onto the antenna during reception

2.3 Monocular Visual Odometry

A variety of vision-based pose estimation algorithms exist, ranging from optical flow measurements to feature tracking to feature recognition techniques [11]. Within this work, a single camera is used that tracks features over consecutive video frames.

In order to derive the pose change between two frames of a video stream, distinct features must be found and tracked. Features can be points, edges, planes or other types [11].

Consider 3-D point P is identified within two consecutively recorded images or video frames labeled with indices 0 and 1 by tracking a feature. The camera, which recorded those images, was located at positions c_0 and c_1. All three points, c_0, c_1 and P define a plane, which is called the epipolar plane.

The projections from P into the image coordinates are labeled p_0 and p_1 respectively. The epipolar constraint can be derived as

$$p_1^T E\, p_0 = 0. \tag{1}$$

Hereby, E is the Essential Matrix, which can be decomposed into

$$E = [t]_x R, \tag{2}$$

where t is the normalized translation vector and R the relative orientation change [11]. By tracking eight or more features between two images, the Eight-Point Algorithm can be used to derive the essential matrix to fulfill Equation (1). Knowing E, the translation and the relative pose change can be calculated by performing Singular Value Decomposition. Here, sequential keyframes of the camera are undistorted, FAST features are tracked and the essential matrix is estimated through Nister's algorithm [15].

Different variations and extensions of VO and the associated challenges are discussed in [16]. The most significant issues and potential solutions are:

- The authors claim that even though optical cameras are providing meaningful information at low cost, image based pose estimation is highly sensitive to effects of outdoor environments. Especially, lighting, illumination changes, blurred images, shadows, water and snow are challenges for VO. Furthermore, forward facing cameras are prone to image disturbances by wind and sunlight driven changes.
- As image based pose change estimation is prone to noise, cumulative errors are introduced within the integrated dimensions analogously to an IMU. However, the authors claim that modern algorithms are relatively more accurate than GPS and Inertial Sensors. The bias drift of VO is generally lower as for low-cost IMUs.
- Furthermore, the authors conclude that monocular VO is easy to deploy as no synchronization has to be implemented as with stereo VO. However, monocular VO suffers from scale uncertainty, i.e. the translation vector t in Equation (2) has a Euclidean norm of 1. Therefore, a simple integration will lead to position solutions, that are ultimately wrong. According to the authors, the absolute scale can be derived through a-priori knowledge of distances of features within the image, motion constraints or through other sensors, e.g. an IMU.
- According to [17], RANSAC a common technique to handle outliers in VO, which is generally prone to noise and outliers. RANSAC, applied to VO, selects a minimal random subset of features to generate a motion hypothesis, e.g. 8 features for the 8-point algorithm. Multiple hypotheses for different random sets are generated and a score is calculated corresponding to how well the hypothesis fits the rest of the observations. The hypothesis with the best score is selected as the winner. With Preemptive RANSAC, the efficiency is increased by avoiding the score calculation of implausible hypotheses.

3 Integrity Monitoring

As introduced in Section 1, requirements are set for navigation systems to qualify for use in aviation. One of these requirements is the integrity of a navigation solution. The ability of a system to detect erroneous navigation solutions and consecutively warn the user is called Fault Detection (FD). More advanced systems may also recover from (FDR), isolate (FDI) or exclude the failures (FDE) and try to resume normal operation [7]. Within this Section, detection methods for faults of individual sensor sources are introduced. Additionally, a test statistic is presented, which is required to determine integrity.

3.1 Measurement Innovation Monitoring

To detect failures of sensors, consistency checks can be performed. Kalman Filter innovations can be filtered (Innovation Filtering) or analyzed using sliding window operations (Innovation Sequence Monitoring). One such consistency check is the well known Receiver Autonomous Integrity Monitoring (RAIM), which is widely used in GNSS receivers. In [18], the range comparison and position comparison methods were presented as two RAIM methods. For the range comparison methods, at least five satellites are required. For each minimal subset of four satellites, the user position is estimated and the pseudo-range of the other satellites are predicted. The difference between the predictions and the true measurements are then used for failure detection.

The measurement innovation δz_k^- of a Kalman Filter and the associated covariance matrix $C_{\delta z,k}^-$ are defined as:

$$\delta z_k^- = z_k - H_k \hat{x}_k^-, \tag{3}$$

$$C_{\delta z,k}^- = H_k P_k^- H_k^T + R_k. \tag{4}$$

The normalized innovation vector y_k can be calculated for each entry j

$$y_{k,j}^- = \frac{\delta z_{k,j}^-}{\sqrt{C_{\delta z,k,j,j}^-}}, \tag{5}$$

which follows a zero-mean unit-variance Gaussian distribution under ideal conditions and values of consecutive epochs are i.i.d.

During periods of large state uncertainties, e.g. during the initial convergence of the filter, the measurement innovations suffer from large oscillations. Additionally, the variance is large, which is the same for noisy measurements during the run-time of the filter. However, faulty measurements, i.e. biases, affect the innovation before the error covariance matrix is updated. Subsequently, immediate large discrepancies can be distinguished from both other situations as peaks of the normalized innovation. A qualitative representation over the run-time of a filter is shown in Figure 2.

When a measurement innovation peak exceeds a predefined threshold, it can be excluded from the Kalman Filter calculation pipeline, which is referred to as Innovation Filtering. For small discrepancies or ramps that grow over time, Innovation Sequence Monitoring can be used. Hereby, the moving average μ_k of the normalized measurement innovation vector is calculated and compared to a sample size dependent threshold.

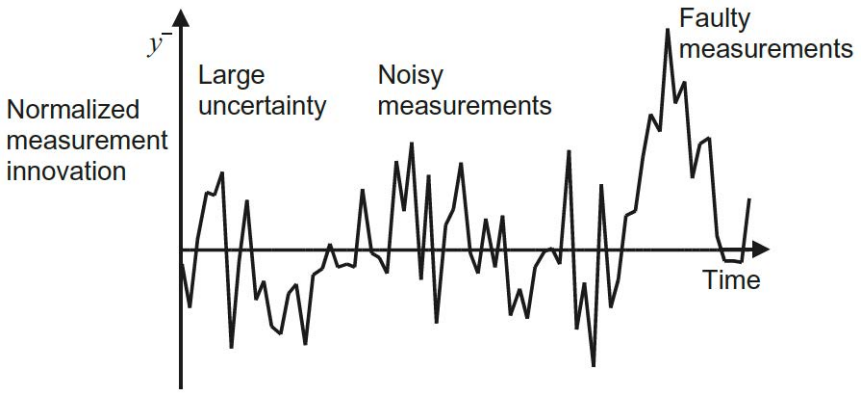

Fig. 2 Qualitative history of normalized measurement innovations during different situations, Source: [7, p. 709]

3.2 Innovation Test Statistic

In order to acquire a test statistic for the whole filter at a given epoch k, the χ^2 distributed test statistic

$$s^2_{\delta z,k} = (\delta z_k^-)^T (C_{\delta z,k^-})^{-1} \delta z_k^- \tag{6}$$

is adopted from [19]. As the innovation is normalized by $C_{\delta z,k^-}$, $s^2_{\delta z,k}$ is unitless, which allows Equation (6) to be applied to filters with innovations comprising different dimensions. As the test statistic, given in Equation (6), is calculated as the sum of squared residuals being Gaussian distributed, it becomes clear that $s^2_{\delta z,k}$ follows a χ^2 distribution. The degrees of freedom, m, correspond to the dimension of the measurement vector. To detect slowly growing faults, batch processing can be performed by calculating the mean residuals over 30 minutes and more [20]. However, as this paper focuses on short term faults in urban environments, Equation (6) is further used.

In the absence of a fault, δz_μ^- follows a zero-mean Gaussian distribution, which makes it possible to state a null- and alternative hypothesis for the fault-free and biased case [19]. The hypotheses can be defined as

$$H_0 : E(\delta z_\mu^-) = 0, \tag{7}$$

$$H_\alpha : E(\delta z_\mu^-) \neq 0. \tag{8}$$

Using the probability relationship

$$P\{s^2_{\delta z,k} < \chi^2_{m,1-\alpha} \| H_0\} = 1 - \alpha \tag{9}$$

with a given significance level α, the null-hypothesis can be accepted or rejected. When rejected, the hypothesis indicates the presence of a fault within the filter.

4 Proposed Navigation Filter

This section presents the architecture, which is followed by the derivation of the individual Kalman Filter models. The first filter follows the design of [7], whereas the second filter is proposed as a novel design. Finally, the selected method for the purpose of integrity monitoring is provided and mode-switching conditions are presented.

4.1 Navigation Filter Architecture

The proposed navigation filter consists of two independent cascaded error-state Kalman Filters, whose outputs can be interchanged, such that the most reliable error estimates are fed back to the INS. An overview of the architecture is given in Figure 3.

The system consists of an IMU, a GNSS receiver and navigation processor providing pseudo-range measurements and SV positions, and a camera. Using a VO algorithm, consecutive camera images are transformed into angular rate and trend vector measurements according to the VO algorithm introduced in Section 2. IMU specific force and angular rate measurements are fed to the INS.

Within the INS, the typical strapdown inertial computations are performed as introduced in Section 2. Before the attitude update and specific force frame transformation are carried out, both measured values, $\tilde{f}^b_{ib}$ and $\tilde{\omega}^b_{ib}$ are corrected for the estimated biases through the closed loop channel as shown in

Figure 3. Furthermore, depending on the filter, the position, velocity and attitude are also corrected, i.e. the previous navigation solution is corrected for the estimated error vector. The inertial navigation solution, consisting of position estimate $\hat{r}^e_{eb}$, velocity estimate $\hat{v}^e_{eb}$ and attitude estimate $\hat{C}^e_{eb}$, is therefore the corrected reference navigation solution.

Both the INS/GNSS EKF and the INS/VO EKF utilize that corrected navigation solution within their structure. A Mode Switching Unit (MSU) continuously monitors integrity conditions of the INS/GNSS filter and can switch to the INS/VO filter, if necessary. Depending on the current operation mode, the INS is corrected by the error-state estimates of either the INS/GNSS Extended Kalman Filter or the INS/VO Extended Kalman Filter. Furthermore, the system gives an output of the overall integrity status of the navigation filter.

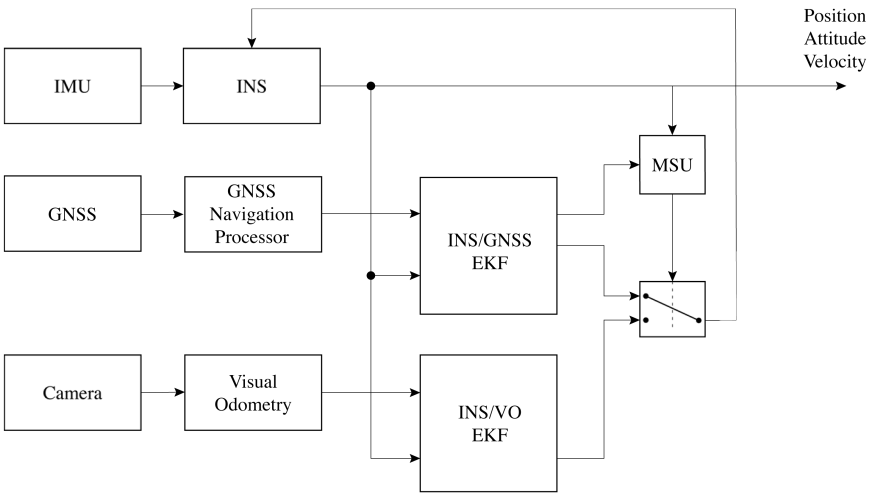

Fig. 3 Proposed filter architecture showing three sensor sources, the two parallel Kalman Filters and the MSU

Following the recommendation of [1] that GNSS shall remain the main source for navigation, the INS/GNSS filter acts as the primary filter as it does not suffer from cumulative errors or drift over time. The INS/VO filter acts as bridging over periods, when the INS/GNSS filter is unavailable or unreliable, which is called coasting. Hereby, the INS/VO filter reduces the drift compared to an INS implementation.

4.2 INS/GNSS Extended Kalman Filter

Within this paper, a modified version of the tightly coupled INS/GNSS integration described in [7] is derived. The integration within the ECEF frame is modified to incorporate multiple and arbitrary constellations but is limited to pseudo-range measurements.

The state vector consists of the attitude error $\delta\psi^e_{eb}$, velocity error δv^e_{eb}, position error δr^e_{eb}, accelerometer bias b_a, gyroscope bias b_ω, GNSS receiver clock bias δc and GNSS receiver clock drift $\delta\dot{c}$. In order to utilize different constellations at once, the clock errors have to be estimated for all L constellations individually. The state vector x can then be modified as

$$x = (\delta\psi^e_{eb}, \delta v^e_{eb}, \delta r^e_{eb}, b_a, b_\omega \mid \delta c_1, \delta\dot{c}_1, \ldots, \delta c_L, \delta\dot{c}_L)^T. \tag{10}$$

The state transition matrix is defined as

$$\Phi = \begin{pmatrix} \Phi_{INS} & 0 \\ 0 & \Phi_{GNSS} \end{pmatrix}, \tag{11}$$

with Φ_{INS} and Φ_{GNSS} given in Appendix 6. Hereby, Φ_{GNSS} is also modified for the multi constellation assumption.

From the GNSS navigation processor, the positions of the SVs are known within the earth frame. By subtracting the corresponding estimated pseudo-ranges from the M measured pseudo-ranges $\tilde{\rho}_1, \tilde{\rho}_2, ..., \tilde{\rho}_M$

at the current epoch, the differences $\delta\tilde{\rho}_s$ are calculated and used as measurement vector for the filter. Measurement vector z is therefore given as

$$z = (\delta\tilde{\rho}_1, \delta\tilde{\rho}_2, ..., \delta\tilde{\rho}_M)^T. \tag{12}$$

This work uses pseudo-range measurements only, not carrier-phase measurements. Therefore, the measurement matrix H_k for M measurements is given by:

$$H_k = \begin{pmatrix} 0_{1,6} & (u_1^e)^T & 0_{1,9} & 1_1 & 0 & \dots & 1_L & 0 \\ 0_{1,6} & (u_2^e)^T & 0_{1,9} & 1_1 & 0 & \dots & 1_L & 0 \\ \vdots & \vdots & \vdots & \vdots & \vdots & & \vdots & \\ 0_{1,6} & (u_M^e)^T & 0_{1,9} & 1_1 & 0 & \dots & 1_L & 0 \end{pmatrix}, \tag{13}$$

where u_m^e is the normalized line of sight vector from the GNSS antenna to the SV and 1_l being only 1, if the measurement is made with a SV of constellation l, i.e. the clock error states of constellation l are correlated with the measurement.

Lack of measurements for one of the constellations can lead to singularities within the Kalman Filter calculations. Therefore, if no measurement is available for GNSS constellation l, the corresponding entries within the H and P matrices and the state vector x are eliminated. Once a new measurement, containing constellation l, is available, the entries will be restored. Depending on the duration of the outage, the process noise matrix P has to account for the grown uncertainty of the clock error states within that duration. For this paper, the default values of initialization are restored in such cases.

Except for the position error, the state vector elements are assumed to be subject to uncorrelated noise according to [7], i.e. there are only entries on the diagonal matrix of the noise covariance matrix Q.

4.3 INS/Visual Odometry Extended Kalman Filter

The error-state INS/Visual Odometry Extended Kalman Filter is a novel design, which is described within this section. The state estimates are the velocity error δv_{eb}^e, attitude error $\delta\psi_{eb}^e$, accelerometer bias b_a and gyroscope bias b_g as given in

$$x = (\delta v_{eb}^e, \delta\psi_{eb}^e, b_a, b_g)^T. \tag{14}$$

To derive the state transition matrix, the propagation of the error state estimates is derived. Neglecting accelerometer bias and noise first, the dependency of the velocity error δv_{eb}^e propagation on the attitude error $\delta\psi_{eb}^e$ can be modeled as

$$\delta\dot{v}_{eb}^e = [\delta\psi_{eb}^e]_x \bar{f}_{ib}^e, \tag{15}$$

where $[\delta\psi_{eb}^e]_x$ is the small angle rotation error of the INS and $\bar{f}_{eb}^e$ is the true specific force corrected for the accelerometer bias. As both specific force $\tilde{f}_{ib}^b$ and accelerometer bias $\hat{b}_a$ are given within the body frame, the estimate of the rotation between body frame and earth frame $\hat{C}_b^e$ from the INS must be applied:

$$\delta\dot{v}_{eb}^e = [\delta\psi_{eb}^e]_x \hat{C}_b^e \bar{f}_{ib}^b \tag{16}$$

In order to bring the equation into the state transition form, the cross-product property of the skew-symmetric matrix $[\cdot]_x$ is utilized, i.e. for two arbitrary vectors $a, b \in \mathbb{R}^3$ the equality $a \times b = -b \times a$ holds:

$$\delta \dot{v}^e_{eb} = -\hat{C}^e_b [\bar{f}^b_{ib}]_x \delta \psi^e_{eb} \tag{17}$$

Furthermore, the velocity error depends on the accelerometer bias b_a and the accelerometer noise w_a, which also need to be rotated from the body frame into the earth frame. Therefore, for the velocity error state propagation, following relationship can be found:

$$\delta \dot{v}^e_{eb} = -\hat{C}^e_b [\bar{f}^b_{ib}]_x \delta \psi^e_{eb} - \hat{C}^e_b b_a - \hat{C}^e_b w_a \tag{18}$$

Note, the actual value of the specific force $\bar{f}$ is not available. According to [8], the following approximation can be made:

$$\bar{f}^b_{ib} \approx \hat{f}^b_{ib} = \tilde{f}^b_{ib} - \hat{b}_a \tag{19}$$

Analogously to the previous process, the attitude error propagation can be analyzed. It is dependent on the attitude error $\delta \psi^e_{eb}$ as well as on the gyroscope bias b_g and the gyroscope noise w_g:

$$\delta \dot{\psi} = [\bar{\omega}]_x \delta \psi^e_{eb} - b_g - w_g \tag{20}$$

Both biases are suffering from dynamic effects as introduced in Section 2. Thus, the bias is modeled as a first-order Gauß-Markov sequence, which is described in [21]. It is characterized by the correlation time constants τ_a and τ_g as well as w_{b_a} and w_{b_g} respectively:

$$\dot{b}_a = -\frac{b_a}{\tau_a} + w_{b_a} \tag{21}$$

$$\dot{b}_g = -\frac{b_g}{\tau_g} + w_{b_g} \tag{22}$$

Ultimately, the system matrix F and system noise distribution matrix G are

$$F = \begin{pmatrix} 0 & -\hat{C}^e_b [\bar{f}^b_{ib}]_x & -\hat{C}^e_b & 0 \\ 0 & [\bar{\omega}]_x & 0 & -I_3 \\ 0 & 0 & -\frac{1}{\tau_a} I_3 & 0 \\ 0 & 0 & 0 & -\frac{1}{\tau_g} I_3 \end{pmatrix}, \; G = \begin{pmatrix} -\hat{C}^e_b & 0 & 0 & 0 \\ 0 & -I_3 & 0 & 0 \\ 0 & 0 & I_3 & 0 \\ 0 & 0 & 0 & I_3 \end{pmatrix}. \tag{23}$$

As measurement vector, the difference between the measured and estimated velocity $\tilde{v}$ and $\hat{v}$ as well as the difference between measured and estimated angular rate $\tilde{\omega}$ and $\hat{\omega}$ are considered. The filter update is performed once every new keyframe is available. Therefore the measurement vector z is given as

$$z = (\tilde{v} - \hat{v}, \tilde{\omega} - \hat{\omega})^T = (\delta \tilde{v}, \delta \tilde{\omega})^T \tag{24}$$

Monocular VO can only measure the velocity $\tilde{v}$ up to a scale, which was introduced as the trend vector $\tilde{t}$ in Section 2. As the Euclidean norm of $\tilde{t}$ is 1, the approximation

$$\tilde{v} = \|\hat{v}\|\tilde{t} \tag{25}$$

was made. Obviously, the assumption introduces a time correlation as $\hat{v}$ is based on the calculation of the previous epoch, while $\tilde{t}$ is measured at the current epoch. However, for low dynamic operations the effect is assumed to be negligible. During the tests, presented in Section 5, no time correlated effects were observed. No noise correlation is considered, i.e. noise covariance matrix Q is a diagonal matrix.

4.4 Integrity Monitoring and Mode-Switching

For both filters, the innovation test statistic from Equation (6) is calculated. Individual significance levels α are selected. If the fault-free hypothesis of the INS/GNSS Extended Kalman Filter is rejected, the MSU switches to the INS/Visual Odometry Extended Kalman Filter. Hereby, the position, attitude and velocity error estimates as well as the bias estimates of the last valid INS/GNSS estimation are given as aiding reference for the INS/VO filter. As both filters run in parallel, the INS/GNSS filter can recover. Upon recovery, the INS/GNSS filter is set as reference navigation filter again. Therefore, the INS/GNSS filter remains the prioritized filter, whereas the INS/VO filter bridges the coasting phases with reduced drift compared to the uncorrected INS. Furthermore, the INS/GNSS Extended Kalman Filter uses Innovation Filtering to detect biases of individual measurements. If a threshold is surpassed by the corresponding normalized innovation, the SV is considered to be faulty and is excluded for a constant period of time T_{exc} from further measurements of the filter.

5 Results

In this sectiion, the chosen hardware is presented and a characteristic test dataset is introduced. The proposed filter is then applied to the dataset and the results are discussed.

5.1 Test Setup

As IMU, the InvenSense consumer grade MEMS IMU ICM-20948 was selected. The monochromatic camera camera consists of the Daheng Imaging Mercury MER-133-54U3M-L body with 1280x960px resolution and a 2mm M12 lense. As multi-constellation and multi-frequency GNSS receiver, the u-blox ZED-F9P was chosen along with the u-blox ANN-MB antenna. An Odroid XU4 single board computer records the measurements with timestamps to assure synchronization of the data. While the IMU measurements are recorded at 100Hz, the camera records at 15Hz and the GNSS measurements are provided once every second. Even though the setup is suitable for online estimation, the data was recorded onto a memory card and analyzed offline only. As no ground truth of the position, attitude or velocity can be determined for an UAV without additional sensors, a setup was planned for a ground vehicle based setup, which is shown in Figure 8 in the Appendix. By reconstructing the actual path, a ground truth trajectory was generated from map sources, which can be used as a measure of the position error during the analysis.

Using the ground vehicle based test setup, different datasets were recorded. A characteristic urban dataset was selected for further analysis. Within the duration of 2:58min, speeds between walking speed and 50km/h were recorded. The track is 1.33km long and consists of five 90 degree turns within the environment of buildings with heights between four and five floors. See a sample camera frame in Figure 7 within the Appendix.

5.2 Analysis

As expected, the INS and the VO Integration, are prone to drift. The former position solution accumulates a position error of 1.9km in the end. Additionally to the drift, the VO Integration suffers from scale ambiguity, i.e. no speed information is available, which causes the position estimation to be unusable.

With the INS/VO Kalman Filter, introduced in Section 4.3, the drift can be significantly reduced to a maximum position error of less than 70m, which can be seen in Figure 4. As shown in Appendix 6, the filter is not fully observable during constant velocity phases, e.g. during the long constant velocity episode of the dataset after the third turn. Therefore, the drift rate is greater within this period.

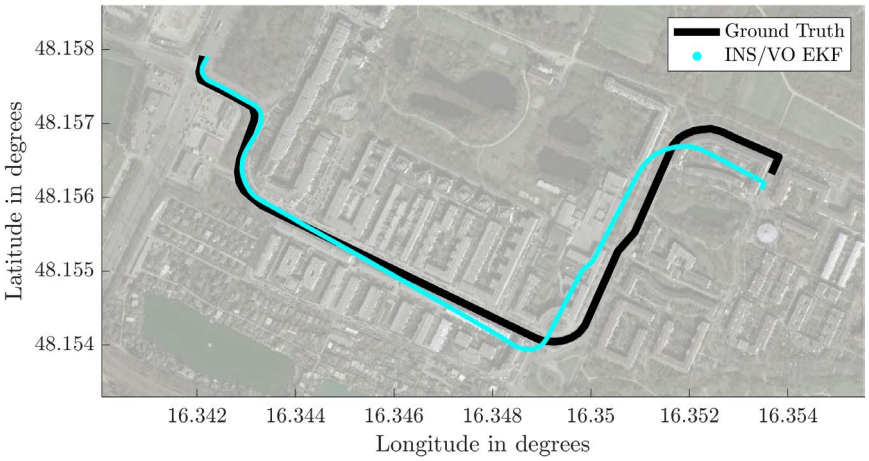

Fig. 4 INS/Visual Odometry Extended Kalman Filter applied to the dataset

The result of the INS/GNSS Extended Kalman Filter without Innovation Sequence Monitoring is shown in Figure 5. Other than VO or an IMU, GNSS based position estimation does not show cumulative errors within the position domain. However, it suffers from noticeable noise in the position domain. Figure 6 shows the result of the proposed filter architecture. Timestamps are shown that indicate the time in seconds from the beginning of the dataset. Based on the dynamically calculated threshold value for the χ^2 test statistic of the INS/GNSS Filter, the INS correction estimation source is either the INS/GNSS Filter or the INS/VO Filter. Position estimations based on the INS/GNSS Filter are shown as magenta points and those based on the INS/VO Filter as cyan points.

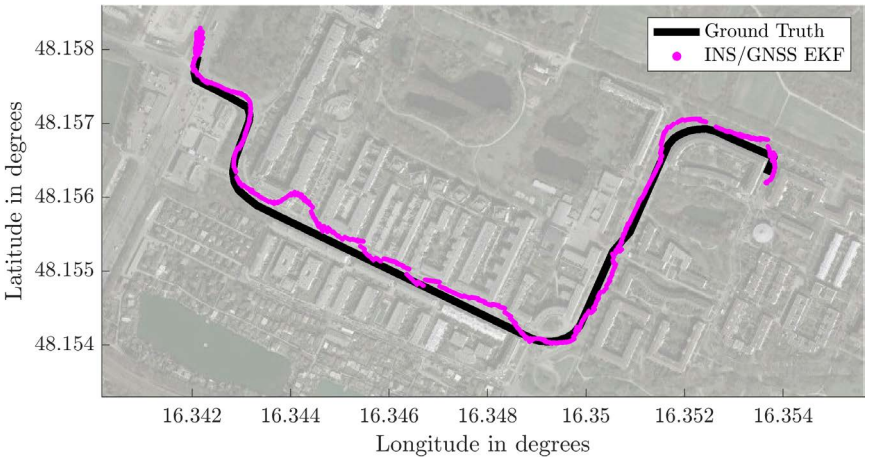

Fig. 5 INS/GNSS Extended Kalman Filter applied to the dataset

It can be seen that the fusion of both filters makes use of the complementary advantages of both architectures. The track estimation is smoother compared to the INS/GNSS filter and it is less affected from drift than the INS/VO filter solution alone. During the Kalman Filter convergence, the INS/VO filter takes over at 10s. The reference is still based on noisy measurements as the Innovation Filtering is not active until an initial convergence. As the reference is noisy and the INS/VO Filter is prone to cumulative errors, the drift until 29s is observable.

Between 37s and 100s, the raw INS/GNSS position estimation is unreliable as shown in Figure 5. As the user enters the shadow of the buildings located south of the road at 37s, which is shown in Figure 1, the signal reception of the satellites with ID 121, 14 and 28 becomes NLOS. The Innovation Filtering excludes these satellites together with those with low elevation angles. Hereby, an exclusion time T_{exc} of

15s is chosen. By excluding pseudo-range measurements of these individual SV, the Innovation Filtering enables a smoother position estimation. Using Innovation Filtering, the pseudo-range residuals remain in a band of $\pm$10m after the initial convergence of the filter. The distributions of the pseudo-range residuals of a satellite can be fitted to a Gaussian distribution. Hereby, the mean is not zero but varies between -2.1m and 3m and the standard deviation is between 3m and 4.2m with a mean of 2.1m.

Both χ^2 hypotheses tests use a significance level α of 5% for the threshold calculation. If a value is greater than zero, the fault-free hypothesis is rejected and the filter integrity can not be ensured. It can be seen that the complementarity of both filters is reflected by the test statistics as some integrity failures are accompanied by low test statistic values of the other filter. Even though the complementary behavior of both filters increases the continuity thereby, there are periods of both statistics being above the threshold. When both filters suffer from a fault-free hypothesis rejection, a dual integrity failure occurs. The duration during which the integrity of both filters can not be guaranteed is 23 seconds of 178 seconds of the total dataset, while the integrity of the INS/GNSS filter alone cannot be ensured for 102 seconds. The continuity could therefore be improved through the parallel filter design.

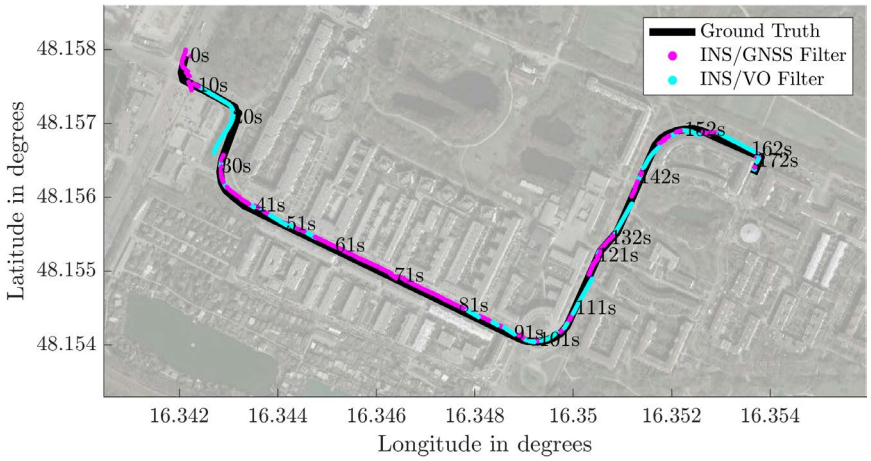

Fig. 6 Results of the combined INS/VO Extended Kalman Filter (cyan colored) and INS/GNSS Extended Kalman Filter (magenta colored) with Innovation Filtering and Mode Switching; Position estimations annotated with timestamp of the dataset

6 Conclusion

With the development of a test setup, a representative dataset was generated to verify the assumed benefits of the proposed filter architecture. Through Innovation Filtering and the subsequent exclusion of individual pseudo-range measurements, the INS/GNSS pose estimation was improved and showed less noise. However, the integrity could not be ensured for over half of the duration of the dataset. Running the INS/GNSS and INS/VO filter in parallel those periods could be bridged and the integrity could be ensured for 87% of the total duration. Additionally, the pose estimation accuracy could be increased compared to the individual filters alone.

As only monocular vision is implemented, the velocity vector measurement is calculated as the scalar multiplication of the measured trend vector with the a-posteriori speed estimate of the previous filter iteration. Therefore, a time dependence was introduced, which could cause errors or even instability of the filter, once the user dynamics are high enough. Even though the dataset was recorded with a ground based vehicle with kinematic constraints, no assumptions were made within the filter algorithms, which makes the results transferable to an UAV. Therefore, future work will focus on proving the benefits of the proposed filter for an UAV.

In summary, this paper presented a novel filter architecture, utilizing GNSS, an IMU and a monocular VO algorithm. Hereby, the complementary advantages were used to improve the integrity and continuity properties of the pose estimation within an urban environment.

Appendix

Representative NLOS Reception - Camera Frame

Fig. 7 Camera frame of the representative NLOS reception at 41s

Observability of the INS/VO Kalman Filter

Observability determines the rate or even ability of the state estimates of a system to converge [21]. The deterministic observability can be shown if the observability matrix M_{DTI} is of rank n, where n is the state vector dimension:

$$M_{DTI}^{T} = \begin{pmatrix} H \\ H\Phi \\ \vdots \\ H\Phi^{n-1} \end{pmatrix} \tag{26}$$

For the further analysis, two representative cases are distinguished.

No Angular Rate

Under the assumption of no angular rate, i.e. the specific force $\bar{f}_{ib}^{b}$ in Equation (23) is any arbitrary acceleration, including 0_3, and the angular rate $\hat{\omega}$ in the same equation is zero. If at least one acceleration component is given, the observability matrix has rank 11, which is a rank deficiency of 1. In cases, where no acceleration is given, the rank is 9. In both cases the system is not fully observable.

Constant Angular Rate

If at least one acceleration and one angular rate component is non-zero, the rank of the observability matrix is 12 and the system is fully observable.

A potential example can be seen in Figure 4, where the position estimations during the first three 90-degree (case 2) turns are relatively drift-free, whereas a constantly growing drift is visible during the turn-free track thereafter (case 1).

Vehicle Based Test Setup

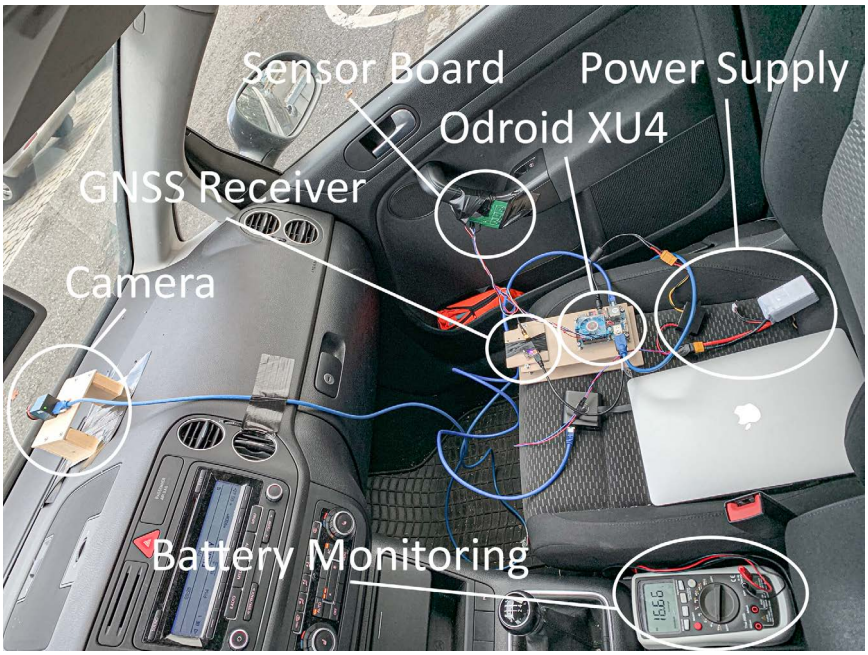

Fig. 8 Test setup for the ground vehicle based recordings

INS/GNSS State Transition Matrix

The state transition matrix of the INS is adopted from [7]:

$$\Phi_{INS} = \left(\begin{array}{ccc|ccccc} I_3 - \Omega^e_{ie}\tau_s & 0_3 & 0_3 & 0_3 & \hat{C}^e_b\tau_s & \dots & 0_3 & \hat{C}^e_b\tau_s \\ F^e_{21}\tau_s & I_3 - 2\Omega^e_{ie}\tau_s & F^e_{23}\tau_s & \hat{C}^e_b\tau_s & 0_3 & \dots & \hat{C}^e_b\tau_s & 0_3 \\ 0_3 & I_3\tau_s & I_3 & 0_3 & 0_3 & \dots & 0_3 & 0_3 \\ 0_3 & 0_3 & 0_3 & I_3 & 0_3 & \dots & I_3 & 0_3 \\ 0_3 & 0_3 & 0_3 & 0_3 & I_3 & \dots & 0_3 & I_3 \end{array}\right) \tag{27}$$

Hereby, matrices F^e_{21} and F^e_{23} are given as

$$F^e_{21} = [-(\hat{C}^e_b \hat{f}^b_{ib})]_x, \tag{28}$$

$$F^e_{23} = -\frac{2\hat{\gamma}^e_{ib}(\hat{r}^e_{eb})^T}{r^e_{eS}(\hat{L}_b)|\hat{r}^e_{eb}|}, \tag{29}$$

where $\hat{\gamma}^e_{ib}$ is the estimated gravity and $\hat{r}^e_{eS}(\hat{L}_b)$ the estimated latitude dependent estimate of the geocentric radius at the surface of the earth [7].

The transition matrix of the GNSS related states is modified from the matrix given in [7]. To take L different constellations into account, the matrix Φ_{GNSS} of [7] has to be given for every constellation. Therefore, the state transition matrix can be constructed from the original state transition matrix proposed by Groves $\Phi^{'}_{GNSS}$ as

$$\Phi_{GNSS} = \begin{pmatrix} \Phi'_{GNSS,1} & & 0 \\ & \ddots & \\ 0 & & \Phi'_{GNSS,L} \end{pmatrix}. \tag{30}$$

Hereby, $\Phi'_{GNSS,l}$ is independent from the constellation and given by Groves as

$$\Phi'_{GNSS,l} = \begin{pmatrix} 1 & 0 \\ \tau_s & 1 \end{pmatrix}. \tag{31}$$

Acknowledgments

This work was done in cooperation between the e-VTOL startup VOLARE GmbH and the Institute of Flight Guidance and Air Transport at the TU Berlin. All tests were performed on hardware, which was provided by VOLARE GmbH.

References

[1] Oguz Kagan Isik, Juhyeon Hong, Ivan Petrunin, and Antonios Tsourdos. Integrity Analysis for GPS-Based Navigation of UAVs in Urban Environment. *Robotics*, 9(3):1–20, 2020. DOI: 10.3390/robotics9030066.

[2] International Civil Aviation Organization. ICAO Doc 9613, Performance-based Navigation (PBN) Manual. Technical report, International Civil Aviation Organization, Montreal, 2008.

[3] Airbus S.A.S. The Blueprint for the Sky: The roadmap for the safe integration of autonomous aircraft, 2018.

[4] Tao Jiang, Jared Geller, Daiheng Ni, and John Collura. Unmanned Aircraft System traffic management: Concept of operation and system architecture. *International Journal of Transportation Science and Technology*, 5(3):123–135, 2016. DOI: https://doi.org/10.1016/j.ijtst.2017.01.004.

[5] Federal Aviation Administration. *Concept of Operations v2.0*, second edition edition, 2 2020.

[6] Derek Chen and Grace Xingxin Gao. Probabilistic graphical fusion of LiDAR, GPS, and 3D building maps for urban UAV navigation. *NAVIGATION*, 66(1):151–168, 2019. DOI: https://doi.org/10.1002/navi.298.

[7] Paul D. Groves. *Principles of GNSS, Inertial, and Multisensor Integrated Navigation Systems*. Artech House, Boston, second edition edition, 2013.

[8] Jan Wendel. *Integrierte Navigationssysteme*. Oldenbourg Wissenschaftsverlag GmbH, München, second edition edition, 2011.

[9] Mitchell J. Narins, Leo V. Eldredge, Per Enge, Sherman C. Lo, Michael J. Harrison, and Randy Kenagy. Alternative Position, Navigation, and Timing: The Need for Robust Radionavigation. In Lance A. Davis, Per K. Enge, and Grace X. Gao, editors, *Global Navigation Satellite Systems: Report of a Joint Workshop of the National Academy of Engineering and the Chinese Academy of Engineering*, pages 119–135. The National Academies Press, Washington, DC, 2012.

[10] Shuai Han, Zijun Gong, Weixiao Meng, Cheng Li, and Xuemai Gu. Future Alternative Positioning, Navigation, and Timing Techniques: A Survey. *IEEE Wireless Communications*, 23(6):154–160, 2016. DOI: 10.1109/MWC.2016.1500181RP.

[11] Richard Szeliski. *Computer Vision Algorithms and Applications*. Springer Verlag, London; New York, 2011.

[12] Peter Corke. *Robotics, Vision and Control: Fundamental Algorithms in MATLAB*. Springer International Publishing, Incorporated, Berlin, Heidelberg, 2017.

[13] Richard B. Langley, Peter J. G. Teunissen, and Oliver Montenbruck. Introduction to GNSS. In Peter J.G. Teunissen and Oliver Montenbruck, editors, *Handbook of Global Navigation Satellite Systems*, pages 3–23. Springer International Publishing, 2017.

[14] Paul D. Groves. Shadow Matching: A New GNSS Positioning Technique for Urban Canyons. *Journal of Navigation*, 64(3):417–430, 2011. DOI: 10.1017/S0373463311000087.

[15] D. Nister. An efficient solution to the five-point relative pose problem. *IEEE Transactions on Pattern Analysis and Machine Intelligence*, 26(6):756–770, 2004. DOI: 10.1109/TPAMI.2004.17.

[16] Mohammad O. A. Aqel, Mohammad H. Marhaban, M. Iqbal Saripan, and Napsiah Bt. Ismail. Review of visual odometry: types, approaches, challenges, and applications. *SpringerPlus*, 5(1):1–26, 10 2016. DOI: 10.1186/s40064-016-3573-7.

[17] David Nistér. Preemptive RANSAC for Live Structure and Motion Estimation. In *International Conference on Computer Vision*, number 9, pages 199–206. IEEE Computer Society, 2003.

[18] Young C. Lee. Analysis of Range and Position Comparison Methods as a Means to Provide GPS Integrity in the User Receiver. *Proceedings of the 42nd Annual Meeting of The Institute of Navigation (1986)*, pages 1–4, June 1986.

[19] Mathieu Joerger, Fang-Cheng Chan, and Boris Pervan. Solution Separation Versus Residual-Based RAIM. *NAVIGATION*, 61(4):273–291, 2014. DOI: 10.1002/navi.71.

[20] John Diesel and Sherry Luu. GPS/IRS AIME: Calculation of Thresholds and Protection Radius Using Chi-Square Methods. *Proceedings of the 8th International Technical Meeting of the Satellite Division of The Institute of Navigation (ION GPS 1995)*, pages 1959–1964, September 1995.

[21] Peter S. Maybeck. *Stochastic Models, Estimation, and Control*, volume 1. Academic Press, New York; San Francisco; London, 1979.